Systematic mapping of cell wall mechanics in the regulation of cell morphogenesis

Valeria Davì[a], Louis Chevalier[a], Haotian Guo[a,1], Hirokazu Tanimoto[a,2], Katia Barrett[a], Etienne Couturier[b], Arezki Boudaoud[c,3], and Nicolas Minc[a,3]

[a]Institut Jacques Monod, CNRS, Université de Paris, 75205 Paris Cedex 13, France; [b]Laboratoire Matières et Systèmes Complexes, UMR 7057, CNRS, Université de Paris, 75205 Paris Cedex 13, France; and [c]Reproduction et Développement des Plantes, École Normale Supérieure de Lyon, Claude Bernard Lyon I, Inra, Université de Lyon, CNRS, 69364 Lyon Cedex 07, France

Edited by David A. Weitz, Harvard University, Cambridge, MA, and approved June 3, 2019 (received for review November 30, 2018)

Walled cells of plants, fungi, and bacteria come with a large range of shapes and sizes, which are ultimately dictated by the mechanics of their cell wall. This stiff and thin polymeric layer encases the plasma membrane and protects the cells mechanically by opposing large turgor pressure derived mechanical stresses. To date, however, we still lack a quantitative understanding for how local and/or global mechanical properties of the wall support cell morphogenesis. Here, we combine subresolution imaging and laser-mediated wall relaxation to quantitate subcellular values of wall thickness (h) and bulk elastic moduli (Y) in large populations of live mutant cells and in conditions affecting cell diameter in the rod-shaped model fission yeast. We find that lateral wall stiffness, defined by the surface modulus, $\sigma = hY$, robustly scales with cell diameter. This scaling is valid across tens of mutants spanning various functions—within the population of individual isogenic strains, along single misshaped cells, and even across the fission yeasts clade. Dynamic modulations of cell diameter by chemical and/or mechanical means suggest that the cell wall can rapidly adapt its surface mechanics, rendering stretched wall portions stiffer than unstretched ones. Size-dependent wall stiffening constrains diameter definition and limits size variations; it may also provide an efficient means to keep elastic strains in the wall below failure strains, potentially promoting cell survival. This quantitative set of data impacts our current understanding of the mechanics of cell walls and its contribution to morphogenesis.

cell shape | cell wall | cell surface mechanics | fission yeast

The cell wall (CW) is a ubiquitous structural layer defining the surface properties of most microbial and plant cells (1–3). It is composed of long cross-linked sugar strands and proteins, which form a polymeric matrix typically 10 nm to 1 μm thick. The mechanical properties of the CW are largely determined by its thickness and geometry and by the composition and arrangement of its polymeric network, which impinge on material anisotropy and bulk elasticity (4–6). Those properties are patterned from the biochemistry of wall synthesis and remodeling, which is spatially and temporally regulated during cell growth (5). At short time scales, the CW exhibits elasticlike properties and is put under tension by a large internal turgor pressure typical of walled cells (7–9). As such, the balance between turgor values and wall stiffness has long been predicted to influence the instantaneous shapes of walled cells (10–12). Given the large range of shapes and sizes spanned by walled cells, addressing mechanical strategies and dose-dependent modulations of wall properties remains an outstanding problem in morphogenesis.

Measuring the mechanical properties of the CW has been a long-term endeavor in plant and microbial sciences. Methods to measure wall stiffness include atomic force microscopy (13), active cell bending or compression (7, 8, 14), and strain-stress assays through the modulation of turgor pressure (10, 11, 15–17). These methods allow the determination of surface elasticity but do not account for putative global or local variations in wall thickness, thereby preventing the contributions to CW mechanics from bulk properties vs. thickness from being discerned. This has limited our appreciation of wall mechanical and biochemical regulation, as bulk elasticity likely reflects polymer composition and cross-linking, whereas thickness is expected to depend on a balance between synthesis and deformation rates (5, 16). In addition, those individual parameters have a differential impact on the stress, elastic strain, or bending modulus of the wall (12). Therefore, addressing how individual mechanical parameters locally and globally vary with cell shape and size is essential for a complete conceptual understanding of the contribution of wall mechanics to morphogenesis.

Here, we combined subresolution imaging of CW thickness and laser-mediated wall relaxation assays to systematically map bulk elasticity and thickness, with subcellular resolution and medium throughput. We use this approach to address how mechanical properties of the lateral CW of rod-shaped fission yeast cells vary with cell diameter. Using libraries of shape mutants, we find that the wall is systematically stiffer in wider cells and in wider subcellular regions of misshaped cells. We evidence a wall stiffening mechanism, associated with dynamic diameter increase, in which wall sections become gradually stiffer as they are deformed laterally. Size-dependent wall stiffening maintains elastic strains in the wall to low and near-constant values and constrains diameter definition, with crucial implications for cell viability and size regulation.

Significance

The cell wall is a thin polymeric layer encasing the membrane of bacterial, fungal, and vegetal cells, which supports viability and defines cell shape and the mode of growth and division. The material properties of the cell wall are thus key for understanding morphogenesis, but remain difficult to quantify. We introduce a systematic method to map subcellular values of cell wall thickness and bulk elasticity in large populations of yeast cells with unprecedented accuracy. By screening libraries of mutants with defects in cell shapes, we demonstrate that cell walls are stiffer in larger cells or larger cell portions. This size-dependent stiffening constrains cell size definition and promotes cell mechanical integrity.

Author contributions: V.D., A.B., and N.M. designed research; V.D., L.C., H.G., and K.B. performed research; H.T. and E.C. contributed new reagents/analytic tools; V.D., L.C., H.G., H.T., K.B., and E.C. analyzed data; and V.D., A.B., and N.M. wrote the paper.

The authors declare no conflict of interest.

This article is a PNAS Direct Submission.

[1]Present address: Center for Research and Interdisciplinarity, Université de Paris, 75004, Paris, France.

[2]Present address: Department of Materials Science, Yokohama City University, Yokohama, 236-0004, Japan.

[3]To whom correspondence may be addressed. Email: Arezki.Boudaoud@ens-lyon.fr or nicolas.minc@ijm.fr.

This article contains supporting information online at www.pnas.org/lookup/suppl/doi:10.1073/pnas.1820455116/-/DCSupplemental.

Published online June 24, 2019.

Results

A Medium-Throughput Method to Map Subcellular Mechanical Properties of the CW. The fission yeast *Schizosaccharomyces pombe* is one of the most established models to understand the emergence of cell morphogenesis (18–21). These are rod-shaped cells that grow by tip extension with a near-constant diameter of ∼4 μm. As for other walled cells, their shape is defined by their CW encasing the plasma membrane (5). Building on previous methodologies to map CW thickness and compute its surface stiffness (10, 11, 15, 16), we sought to develop a systematic approach to map those key mechanical parameters in populations of cycling cells and mutants (Fig. 1*A*). We constructed strains expressing GFP-Psy1 to label the plasma membrane at the inner side of the wall, and added specific lectins tagged with a far-red fluorophore to mark the outer face of the wall. As previously reported, this labeling, combined with a dedicated image analysis pipeline, allows the mapping of CW thickness around a given cell, as well as the delineation of CW shape, with nanometric resolution (16) (Fig. 1*B*). After imaging a cell to compute wall thickness, we immediately deflated it by piercing the wall with an ultraviolet (UV) laser focused at a diffraction-limited point on the cell surface (11, 15, 22). Cells deflated with a marked and homogenous reduction in the lateral radius, as well as with changes in curvature at cell tips. Cell shape analysis before and less than 1 min after ablation allowed computing the local value of the ratio of the surface modulus of the CW to turgor pressure, hY/P, where h is wall thickness, Y is bulk elastic modulus, and P is pressure (11) (Fig. 1*C*). This computation was done by using simple analytical expressions for the simple geometries of cylindrical sides and hemispherical tips (11), which were validated using numerical resolutions of the partial differential equations governing axisymmetric thin elastic shells, on a range of geometries covering experimental data (10) (see *Materials and Methods* and *SI Appendix*, Fig. S1 *C–L*, Table S1, and *Supplemental Methods*). In more complex geometries, such as at birth scars, extraction of local elastic moduli was solely achieved using the simulations (Fig. 1*D*). The combination of both methods thus served to independently compute wall bulk elastic moduli and thickness and to test their contribution to morphogenesis.

In wild-type (WT) cells, this approach yielded near-similar mean values of bulk elastic moduli of ∼50 MPa using previous estimates of turgor pressure of 1.5 MPa (7, 10, 11, 16). Locally, the growing old end and the new end after new end take off (NETO) were the softer parts of the cell, likely accounting for growth and wall remodeling there. The birth scars, cell sides, and nongrowing new ends had a bulk elasticity typically ∼2 times higher than growing ends. Sorting cells by length revealed that the old end and cell sides kept near-constant bulk and surface elastic moduli throughout the cell cycle. In contrast, the new end underwent a marked 2-fold reduction in bulk and surface moduli at a length of around 10 to 12 μm, likely corresponding to growth resumption there after NETO (Fig. 1 *D–F*, and *SI Appendix*, Fig. S1 *K* and *L*).

We next asked if local cell shape features were correlated with specific CW mechanical parameters around the cell. Because normal haploid WT cells have a narrow range of diameters, we used starved cells, cells grown at 36 °C, and diploids—conditions known to affect cell diameters. This analysis showed that the local radius of curvature at the old end was only mildly correlated with either CW thickness or elastic and surface moduli divided by pressure. Similarly, new end radii exhibited weak positive correlation with their local counterpart values of bulk and surface moduli, but exhibited no correlation with thickness. In contrast, the radius along the cylinder exhibited the highest positive correlation with side surface moduli, indicating that this mechanical parameter could encode for diameter regulation (Fig. 1 *G–J* and *SI Appendix*, Fig. S2).

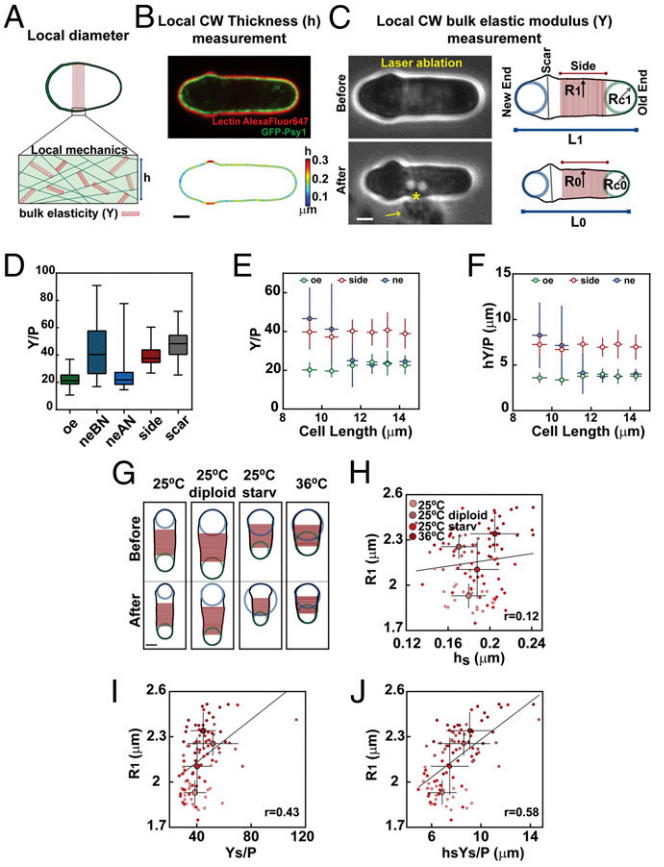

Fig. 1. A method to compute local CW mechanical properties in *S. pombe* cells. (*A*) Schematic of a cell with varying diameters, with enlarged view of local CW organization defining thickness (h) and bulk elastic modulus (Y). (*B*) Midslice confocal image of a cell expressing GFP-Psy1 and labeled with lectin GS-IB$_4$–Alexa Fluor 647 (*Upper*), and the corresponding CW thickness map (*Lower*). (*C*, *Left*) Method to estimate local wall bulk modulus divided by turgor pressure. Bright-field images of the same cell depicted in *B* before (*Upper*) and after (*Lower*) laser ablation. The asterisk indicates the laser-ablating spot; the arrow points at a cloud of ejected cytosolic material. (*C*, *Right*) CW boundaries of the same cell before (*Upper*) and after (*Lower*) ablation, used to compute local radii of curvature at cell tips and the radius along the cell side, defined as a mean on the red region. (*D*) Y divided by turgor pressure (P) values computed at old end (oe, $n = 99$), new end before (neBN, $n = 20$), and new end after (neAN, $n = 64$) NETO, and at sides ($n = 99$) and scars ($n = 27$) in a WT population. (*E* and *F*) Evolution of Y/P (*E*) and hY/P (*F*) as a function of cell length. Individual cells have been imaged and binned by length (between 8 and 20 cells for each point). (*G*) CW boundaries, before and after ablation, of typical WT haploid and diploid cells, and haploid cells after 16 h of starvation (25 °C starv) and at 36 °C in exponential phase. (*H–J*) Cell radius (R_1) plotted as a function of side wall thickness (h_s), side bulk modulus divided by pressure (Ys/P), or surface modulus divided by pressure (hsYs/P) (for 25 °C, $n = 21$; 25 °C diploid, $n = 19$; 25 °C starv, $n = 34$; and 36 °C, $n = 24$). Small dots correspond to single cells, and larger dots are mean values. The line is a linear fit on single-cell measurements. *r* values are Pearson correlation coefficients. Whisker plots represent median and full dataset range. Error bars are SDs. (Scale bars, 2 μm.)

The Surface Modulus of the Lateral CW Scales with Cell Diameter. Building on those observations, we asked whether mechanical properties of the CW would vary in populations of mutants with defective diameter regulation. For this, we examined 26 mutants knocked out for a single open reading frame (ORF), which have been reported to bear defects in cell diameter from previous visual screens of the fission yeast knockout (KO) library (20, 21). After careful validation and diameter quantification, we refocused our analysis on a specific set of 18 mutants that solely exhibited diameter misregulation, discarding more complex misshaped mutants

with other bent or branched features, for instance (20, 21). Importantly, these 18 mutants covered several physiological processes, including polarity, chromosome segregation, metabolism, and wall synthesis (Fig. 2 *A–E* and *SI Appendix*, Fig. S3*A* and Table S2). Defects in diameter regulation in these strains could be segregated into 3 categories. One first category had a mean diameter significantly different (higher or lower) than WT. A second category had a similar mean value to WT diameters, but a much larger variability (computed as a SD), likely reflecting defects in diameter maintenance through successive divisions. A last category was composed of skittle-shaped mutants with defects in diameter along a single cell (Fig. 2 *A–D*). Finally, we added to this screen 8 mutants involved in CW regulation that do not have major defects in diameter but are expected to misregulate wall mechanics. To compute wall mechanical parameters, mutant strains were transformed to stably express GFP-Psy1, and grown and assayed as controls following a standardized procedure. For each strain, we typically analyzed ∼20 to 30 cells, discarding dividing cells. In addition, although we kept mutants that may have skittle-shaped cells, we first analyzed a subpopulation in those strains with near-intact rod shapes.

This analysis, over tens of mutants, revealed a relatively narrow distribution of side CW thickness of around 200 nm, with one particular mutant, *kin1Δ*, exhibiting a significantly higher thickness of more than 300 nm (23) (Fig. 2*F*). Correlation between diameter and thickness was positive but relatively low ($r = 0.39$, Fig. 2*F*). To compute bulk moduli, we first validated the use of analytical expressions by a direct comparison with simulations in a range of representative cells. Using those expressions, we computed elastic moduli divided by pressure, Y/P, and found that they also increased with cell diameter but displayed a much higher correlation ($r = 0.73$, Fig. 2*G*, and *SI Appendix*, Fig. S3 *B–F* and Table S1). Importantly, these variations in the values of Y/P mostly reflected changes in the bulk modulus of the wall, and not turgor pressure. This was evidenced by comparing the relaxed length obtained from wall piercing through laser ablation to that obtained with increasing amounts of sorbitol hyperosmotic treatment (11). This analysis, performed in mutants with the largest diameters, yielded a relative pressure compared with that of WT cells and revealed variations of less than a few percentage points (*SI Appendix*, Fig. S3 *G* and *H*). This suggests that mutants with varying diameters may have similar turgor values and that shape variations may be mostly associated with changes in CW mechanics.

The surface modulus exhibited the highest correlation coefficient with the cell radius ($r = 0.82$, Fig. 2*H*). Accordingly, mutants that departed from the main trend in thickness or bulk elastic modulus appeared to compensate the other parameter so that the surface modulus remained in the mean trend (Fig. 2 *F–H*). We also found a good correlation of thickness and bulk and surface moduli at the old end to that at cell sides, suggesting that mechanical properties of the lateral CW could be defined during the initial synthesis of the CW at cell tips and be modified in the same manner during growth. In contrast, the mechanical properties of the CW at the new end were much less correlated with that of the sides, plausibly as a consequence of prior septum synthesis there (11) (*SI Appendix*, Fig. S4). Thus, this large-scale analysis suggests a dose-dependent link between cell diameter and CW surface modulus, which best represents the stiffness of this structure.

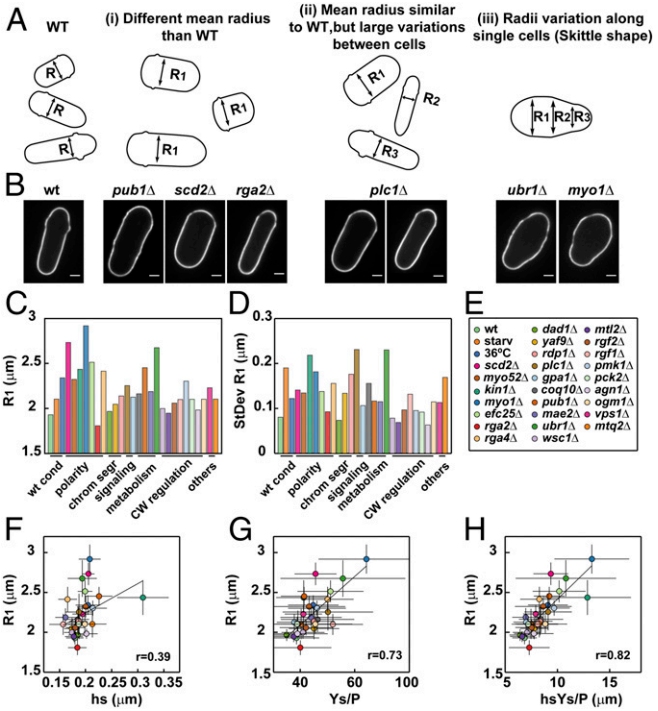

Fig. 2. Mapping CW mechanics in populations of mutants defective in cell diameter. (*A*) Schematic of cell outlines for WT and 3 classes of diameter mutants, with defects in intercellular average radius (*i*), intercellular variance of the radius (*ii*), or in intracellular variance of the radius (*iii*). (*B*) Midslice confocal image of representative cells corresponding to the classes shown in *A*. (Scale bars, 2 μm.) (*C–E*) Mean cell radius on cell sides of different mutants and conditions (*C*) and SDs (StDev) (*D*) as annotated in the legend (*E*). (*F–H*) Cell radius (R_1), plotted as a function of side wall thickness (hs), side bulk modulus divided by pressure (Ys/P) or side surface modulus divided by pressure (hsYs/P), in the conditions and mutants listed in the legend (*E*). Each strain is represented by its mean value. The line is a linear fit on mean values. *r* values are Pearson correlation coefficients.

Size-Dependent Wall Stiffening in Isogenic Populations, at Subcellular Levels, and across the Fission Yeast Clade. We next reexamined a mutant strain, *plc1Δ*, deleted for a gene that encodes for a phospholipase C enzyme and exhibits rod-shaped cells with a high SD in diameter (Fig. 2 *A–E*) (24). When analyzed at the level of a population of single mutant cells, we found a net positive correlation between CW surface modulus and cell diameter. Importantly, this correlation was mostly associated with an increase in bulk modulus of the wall of fatter cells (Fig. 3*A* and *SI Appendix*, Fig. S5 *A* and *B*). Thus, modulation of CW stiffness is associated with cell-to-cell variations in diameter in an isogenic population.

To understand if this correlation was also valid at a local level, we analyzed skittle-shaped cells. We selected 2 representative mutants with skittlelike defects but pertaining to distinct genotypic classes (*myo1Δ* and *ubr1Δ*), and used *plc1Δ* rod-like cells as controls. We computed local diameters along the cell's long axis and plotted them as a function of local surface moduli. While points in the rod-shaped *plc1Δ* cell clustered around a single value, local radii and surface moduli varied and were strongly correlated along the length of single *myo1Δ* and *ubr1Δ* cells, with larger portions of the CW being stiffer. These local estimations were also validated by simulating the inflation of relaxed walls based on our axisymmetric thin-shell model, yielding to near-similar turgid cell shapes (Fig. 3*B* and *SI Appendix*, Fig. S5 *C–E*). Those subcellular effects further rule out putative contributions from turgor variations and suggest that the surface modulus of the CW provides a robust predictor for local as well as global diameters in fission yeast.

Finally, we also measured CW mechanics in closely related species pertaining to the fission yeast clade: *Schizosaccharomyces japonicus*, *Schizosaccharomyces octosporus* and *Schizosaccharomyces cryophilus*. These species exhibit cells with markedly different diameters compared with *S. pombe* cells. Remarkably, the scaling between surface moduli and diameters was also highly pronounced in this clade (Fig. 3 *C* and *D*). However, in contrast to *S. pombe* mutants, variations in stiffness were mostly associated to thickness changes of the lateral wall, with some large *S. japonicus*

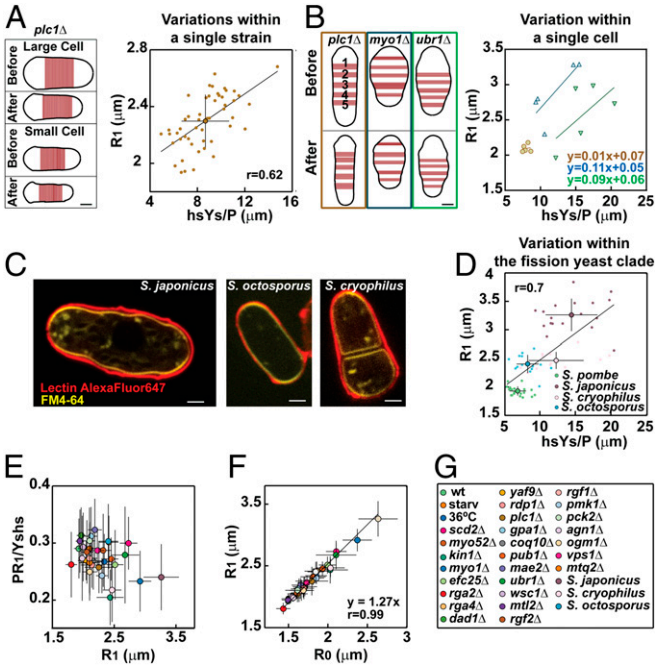

Fig. 3. Estimation of CW mechanical parameters in a single isogenic strain, along single misshaped cells, and in other fission yeast species. (*A*, *Left*) CW boundaries, before and after ablation, of 2 *plc1Δ* cells with large and small radii. (*A*, *Right*) Cell radius (R_1) plotted as a function of the surface modulus divided by pressure (hsYs/P) for a population of *plc1Δ* cells ($n = 50$). (*B*, *Left*) CW boundaries and CW portions on cell sides, before and after ablation, for a rod-shaped cell (*plc1Δ*) and 2 skittle-shaped cells (*myo1Δ* and *ubr1Δ*). (*B*, *Right*) Local radius (R_1) plotted as a function of the surface modulus divided by pressure (hsYs/P) in 5 different parts of the same cell, for the cells in *B*, *Left* (colors of the boxes correspond). (*C*) Representative midslice confocal images of a cell from each species labeled with FM4-64 and lectin GS-IB_4–Alexa Fluor 647. (*D*) Cell radius (R_1) plotted as a function of side wall surface modulus divided by pressure (hsYs/P) for *S. pombe* ($n = 21$), *S. japonicus* ($n = 17$), *S. octosporus* ($n = 14$), and *S. cryophilus* ($n = 12$). (*E*) Elastic strain in the lateral CW ($PR_1/Yshs$) plotted as a function of cell radius. (*F*) Turgid radius (R_1) plotted as a function of the relaxed radius (R_0) in the conditions, mutants, and species listed in *G*. In *A*, *B*, and *D*, lines in plots represent linear fits of single-cell measurements. In *E* and *F*, the line is a linear fit of mean values. *r* values are Pearson correlation coefficients. Error bars represent SDs. (Scale bars, 2 μm.)

cells featuring walls typically twice as thick as *S. pombe* cell walls (*SI Appendix*, Fig. S5 *F* and *G*). This suggests that bulk material properties and plausibly compositions of walls in these different species may not drastically vary. Rather, adaptation of wall thickness appears as the dominant strategy to scale wall stiffness to cell size in the fission yeast clade.

Size-Dependent Lateral Wall Stiffness Limits Elastic Strains. Using the aforementioned data, we then computed which conceptual mechanical parameter may constrain cell diameter definition. We computed the stress born by the lateral CW, defined as PR_1/h_s, the elastic strains defined as PR_1/Y_sh_s, and the bending energy of the CW normalized by that of pressure, computed as $PR_1^3/Y_sh_s^3$, where R_1 is the pressurized radius. Without size-dependent adaptation of wall mechanics, these parameters are expected to increase with diameters. The stress in the CW estimated assuming constant values of pressure of 1.5 MPa systematically increased with diameter. The CW of fatter cells thus bears higher stresses than smaller cells, suggesting that stress limitation may not be a strategy to control the shapes of those walled cells (25). The bending energy was more variable but also increased with diameter, suggesting that CW bending may not constrain diameter definition (12) (*SI Appendix*, Fig. S5 *H–J*). Remarkably, however, we found that the elastic strain in the wall was mostly constant, with values around ∼25 to 30%, and even slightly decreased at larger-diameter values. Accordingly, the relaxed radius, R_0, was strongly correlated with R_1 ($r = 0.99$) so that $R_1 \approx 1.3R_0$, in agreement with a near-constant elastic strain of ∼30% (Fig. 3 *D* and *E*). Thus, this analysis demonstrates that diameter-dependent CW stiffening limits elastic strains in the wall.

Dynamic Modulations of Cell Diameters Reveal Strain-Stiffening Properties of the Lateral CW. Walled cells may undergo rapid shape or size changes. We thus used chemical and physical approaches to dynamically modulate cell diameter and monitor changes in wall mechanics. We first treated cells with a low dose (10 μM) of the actin-depolymerizing drug Latrunculin A (LatA). This intermediate dose may weaken polar domains of the active GTP-bound Cdc42, and yields fatter cells (26). By performing a time course, we noted that cells enlarged their diameters in times as short as 30 to 60 min, without building a whole new CW through growth and division. Rather, the glucan synthase Bgs4 exhibited a gradual dispersion from tips to the whole cell contour over ∼1 h, probably yielding ectopic CW synthesis, remodeling, and diffuse growth, and thereby enlarging diameter (22) (*SI Appendix*, Fig. S6 *A–D*). By computing thickness and bulk elastic moduli in cells treated with 10 μM LatA for 90 min, we found that diameter increase was associated with a reduction of lateral wall thickness, likely resulting from an imbalance between deformation and synthesis (16). This thinning was concomitant with an increase in bulk elastic modulus (Fig. 4 *A* and *B* and *SI Appendix*, Fig. S6 *E* and *F*). Importantly, these changes resulted in a net increase of the surface modulus on cell sides, yielding a near-conservation of CW elastic strains during these dynamic changes in diameter (23% in LatA compared with 26% in dimethyl sulfoxide [DMSO] controls).

As another independent means to dynamically alter diameter, we used microfabricated polydimethylsiloxane (PDMS) channels. We grew large *rga4Δ* mutant cells into narrow microchannels, forcing them to adopt a smaller diameter (27, 28). Remarkably, at the channel exit, cells popped out and recovered their normal large diameters in time scales of a few minutes without growing large portions of new CW. In a subset of experiments, we could even detect cells with one fatter part outside and one thinner part inside the channel. This suggests that the stress exerted by turgor on the CW is partly compensated by the walls of the microchambers, and fully deforms the cell into its normal shape once outside (Fig. 4 *C* and *D* and *SI Appendix*, Fig. S6 *G–I*). Although lateral wall thickness analysis was not compatible with microchannels due to unspecific lectin binding to PDMS walls, we could ablate those cells to measure relaxed radii and elastic strains. This revealed a rapid plastic irreversible deformation of the CW, as the relaxed radius rapidly increased in cells popping out of the channels. In addition, elastic strains were also nearly conserved during this transition, suggesting that expanding walls may rapidly stiffen to limit further expansion (Fig. 4 *E* and *F*).

Those results were indicative of putative strain-stiffening properties of the CW. A signature of materials with such properties is that they compress more than they stretch under an applied mechanical stress of the same magnitude (compressive and tensional, respectively). To assay this, we compared the magnitude of wall deformation in response to hyperosmotic and hypoosmotic shocks of same amplitudes (29). WT cells were rinsed in 1 M sorbitol and left to adapt and recover their turgid state for more than 1 h. Adapted cells had similar wall mechanical properties as normal WT cells (*SI Appendix*, Fig. S7 *A–C*). We then rapidly rinsed those cells either with 2 M sorbitol to create a hyperosmotic shock or with normal media for hypoosmotic shocks, and tracked shape changes within less than 2 or 3 min (Fig. 4*G*). Strikingly, in response to the same pressure difference, cells shrunk significantly more than they inflated. This differential response was also clear

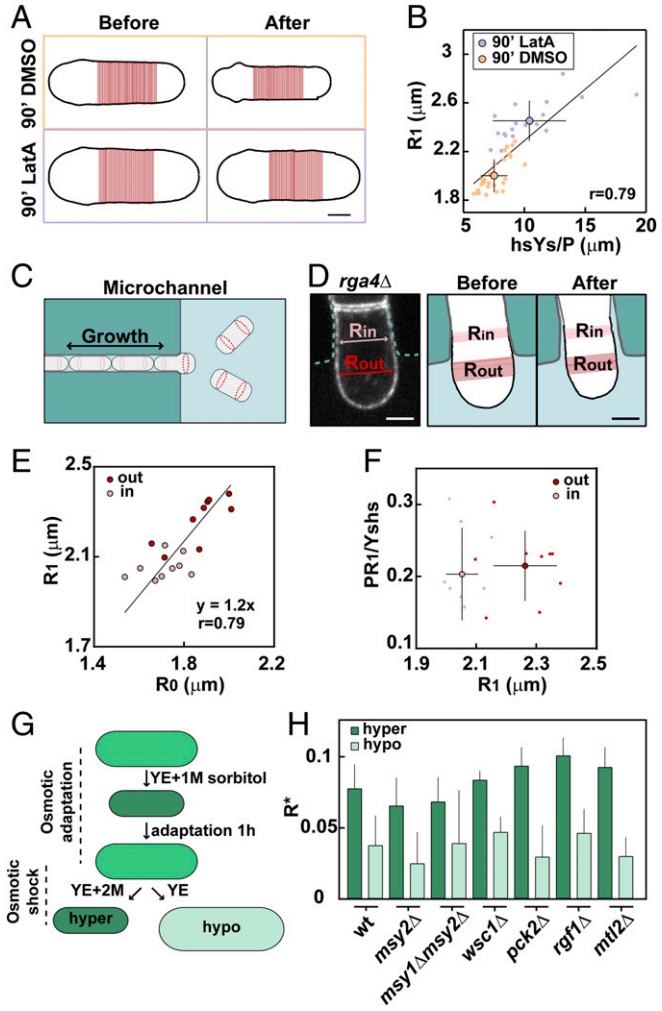

Fig. 4. Dynamic modulations of CW mechanical parameters during local and global shape changes. (*A*) CW boundaries, before and after ablation, of representative cells treated for 90 min with DMSO or 10 μM LatA. (*B*) Cell radius (R_1) plotted as a function of side wall surface modulus divided by pressure (hsYs/P), in WT cells treated with DMSO ($n = 30$) or LatA ($n = 18$). Small dots are single cells; larger dots are averages. The line is a linear fit on single-cell measurements. (*C*) Schematic of cells growing inside a microchannel. (*D*) Midslice confocal image (*Left*) and CW boundaries before and after ablation (*Right*) of an *rga4Δ* cell expressing GFP-Psy1, grown inside a microchannel (cyan dotted line) smaller than the cell radius in this strain (Rin). The part of the cell exiting the channel has a larger radius (Rout). (*E*) Turgid radius plotted as a function of relaxed radius of *rga4Δ* cells ($n = 9$) grown as in *C* and *D*, measured inside (pink) and outside (red) the channel. The line is a linear fit on single-cell measurements. (*F*) Elastic strain in the CW plotted as a function of cell radius in the same cells as in *E*. Small dots are single cells; larger dots are means. (*G*) Schematic of the assay used to apply osmotic shock of similar magnitude but in different directions: cells are placed in YE5S + 1 M sorbitol and left to adapt for 1 h, and then rinsed with either YE5S + 2 M sorbitol to create an hyperosmotic shock or with YE5S for an hypoosmotic shock. (*H*) Relative expansion of radii measured as $(R_{1M} - R_{2M})/R_{1M}$ for hyperosmotic (dark green), or as $(R_{YE} - R_{1M})/R_{1M}$ for hypoosmotic (light green) treatments in the indicated strains ($n = 10$ cells in each conditions). Error bars are SDs. (Scale bars, 2 μm.)

for shocks of lower or higher magnitudes and differed markedly from a simulation with constant CW elasticity (*SI Appendix*, Fig. S7*D* and *Supplemental Methods*). Importantly, this effect was still pronounced in *msy2Δ* or *msy1Δ msy2Δ* mutants defective in turgor adaptation to hypoosmotic stress (30) and in key mutants of the CW integrity pathway (31), indicating that it was mostly independent of canonical downstream wall regulatory signaling (Fig. 4 *G* and *H* and *SI Appendix*, Fig. S7 *E*–*G*). Although these data cannot rule out the implication of unknown wall regulatory systems, they suggest that this effect may involve a rather passive distortion in the wall polymer network, which stiffens strained walls in a dose-dependent manner.

Discussion

By combining wall thickness measurements and relaxation assays, we provide a systematic quantitative assessment of CW mechanical properties in the regulation of single-cell morphogenesis. We find that the CW is globally or locally stiffer in larger cells or cell portions. This scaling remains valid among mutants defective in diverse processes such as polarity, signaling, and metabolism, and in several species of the *Schizosaccharomyces* clade, suggesting that it could represent a broad property of walled cells. This effect has dramatic implications for size regulation. If the largest *S. pombe* mutants had similar stiffness as WT cells, they would reach pressurized diameters of up to 8 to 9 μm instead of 6 μm, and *S. japonicus* cells would reach up to diameters of ∼15 to 20 μm. Interestingly, we find that wall stiffening in *S. pombe* mutants is mostly associated with an increase in bulk elasticity, suggesting that wall polymer composition or arrangement may be directly or indirectly altered by genetic disruptions. In contrast, other fission yeasts appear to adapt stiffness by thickening their lateral wall at a relatively fixed bulk elasticity. The human pathogen *Cryptococcus neoformans* features titan cells typically 10 times larger than normal cells and exhibit a specific thick and stiff polymeric capsule (32). The wall of plant-pathogenic fungi can become melanized to support large size increases associated with appressoria formation (32, 33). Modulation of wall surface stiffness may thus be a conserved strategy for walled cells to cope with size variations.

During dynamic shape changes, we provide significant evidence for the existence of gradual wall stiffening, which renders stretched CW portions stiffer than relaxed ones. Active lateral wall remodeling, such as in LatA experiments, may promote stiffening of enlarging CWs at relatively long time scales (similar to those of growth). However, physical manipulations in microchambers and with osmotic treatments support rapid and plausibly passive strain-stiffening properties of the lateral CW. Similar effects reported in bacteria and plant CWs have been proposed to implicate the passive rearrangement or stretching of individual wall polymers in the direction of deformation, which renders the material stiffer (29, 34). Which particular polymer or cross-link may promote such behavior is an exciting research avenue for the future.

Tip growth is also associated with CW flows that define a time scale for CW expansion and translocation from tips to sides (10, 35). CW expansion might thus also be viewed as a viscous process, whereby the rate of expansion is proportional to CW tension and CW effective viscosity. The cessation of lateral expansion when cell diameter is reached would require viscosity to become very large at the same time as the CW stiffens. We foresee that these mechanical maturations, whether passive or active, could have relevance to normal cell growth, by promoting the gradual stiffening of initially soft CW portions assembled at cell tips as they move along the cylinder during growth. Thus, size-dependent stiffening may confer a unique mechanical benefit to tip-growing cells by limiting lateral size variations while maintaining a relatively soft CW at the tips needed for growth (36).

Finally, size-dependent wall stiffening allows for maintaining elastic strains to relatively constant and low values. Measured elastic strains in our assays do not exceed 25 to 30%, which is below the estimated failure strain of the CW (at which the wall would break open) of ∼45% measured in *Saccharomyces cerevisiae* (14). Although the composition of the CW in *S. pombe* is different, our findings of a conserved strain well below this failure strain suggest that the CW will remain mostly intact, even

when cells are grown to a larger size. Thus, our data support plausible generic mechanical principles of the CW supporting both cell shape and integrity.

Materials and Methods

Yeast Strains, Media, Genetics, and Drug Treatments. Standard methods for *S. pombe* media and genetic manipulations were used. Strains used in this study are listed in *SI Appendix*, Table S3. Diameter mutants were selected from an initial list of 62 misshapen mutants intersecting visual screens of the fission yeast KO library (20, 21). Mutants were either transformed or crossed to generate strains stably expressing GFP-Psy1. Through visual inspection, mutants with cylindrical or quasi-cylindrical shape were selected, excluding more complex phenotypes. Skittle-shape phenotypes were not fully penetrant, allowing for imaging a subset of cylindrical cells in the population. A final quantification was done to select mutants with a larger mean diameter or large variance. LatA (Sigma) was used at a final concentration of 10 μM from a 1000× stock in DMSO.

Microfabricated Chambers. The general design, fabrication, and assembly of microchannels to control fission yeast diameter is described in ref. 22. Spores from a homothallic *rga4Δ* strain were inserted into the PDMS microchannels and left to germinate for >20 h at 25 °C in YE5S plus GS-IB_4–Alexa Fluor 647 conjugate.

Microscopy. In all experiments, cells were prelabeled in YE5S media containing 5 μg/mL of labeled lectin from *Griffonia simplicifolia* (GS-IB_4–Alexa Fluor 647; Thermo Fisher Scientific). For single-time imaging and laser ablation, cells were placed between a glass slide and a coverslip and imaged within 20 min. Time-lapse imaging for LatA and osmotic treatments was performed in homemade glass channels built from one 24 × 50 mm (VWR, Radnor, PA) and a 22 × 22 mm (Thermo Fisher Scientific) coverslip spaced by ∼250 μm, using double-sided tape. The flow channel was first coated with 1 mg/mL poly-L-lysine (Sigma-Aldrich), rinsed, and subsequently coated with 0.1 mg/mL GS-IB_4 (Sigma-Aldrich) and rinsed with water and YE5S, before prelabeled cells were flowed in. Imaging was performed at room temperature (22 to 26 °C) with controlled humidity (>30%). Details for imaging setups and image analysis scripts are reported in *SI Appendix, Supplemental Methods*.

Calculations of Bulk Elastic Moduli from Wall Relaxation Assays. Values of bulk modulus divided by turgor pressure were estimated as in ref. 11, using the variations in cell shape before and after laser ablation and CW thickness maps. Assuming the CW material to be homogenous and isotropic (10, 11), and given that the ratio of radial to longitudinal expansion upon wall ablation is close to 2 (*SI Appendix*, Fig. S1 *A* and *B*), the Poisson's ratio of the CW was taken to be 0. As a consequence, for the simple cylindrical geometry of the cell side, the force balances on the CW yields

$$\frac{Y_{side}}{\Delta P}=\frac{R_1}{h_{side}R_1^*},$$

where $R_1^*=\frac{R_1-R_0}{R_0}$, with R_0 being the deflated radius on cell sides. At cell tips, force balance reads as

$$\frac{Y_{tip}}{\Delta P}=\frac{Rc}{2h_{tip}Rc^*},$$

where $Rc^*=\frac{Rc-Rc_0}{Rc_0}$, with Rc_0 being the deflated curvature radius at cell tips.

As stated throughout the manuscript, these analytical formulae were validated with a numerical resolution of the partial differential equations governing thin elastic shells (10) (*SI Appendix, Supplemental Methods* and Fig. S1 *C–L*). When local cell shapes were not perfectly cylindrical (e.g., in the analysis of bulk moduli at birth scars, Fig. 1*D*), we derived values using this computational approach only. Those simulations were also used to confirm results in cells with varying diameters and in skittlelike cells (*SI Appendix*, Figs. S1*K*, S3 *B–F*, and S5*E*). Finally, we note that laser ablation could leave some remnant of pressure (11). Although this effect could slightly alter the exact values of bulk moduli, it would not affect the ratio of moduli to pressure reported throughout this work.

ACKNOWLEDGMENTS. We acknowledge Y. Sanchez, T. Toda, P. Perez, H. Lida, and N. Rhind for sharing material. We thank S. Dmitrieff, A. Haupt, and other members of the N.M. laboratory. We acknowledge the ImagoSeine facility, a member of France BioImaging (ANR-10-INSB-04). This project was supported by the CNRS and grants from the Seventh Framework Program Career Integration Grant (FP7 CIG) program, the Initial Training Network (ITN, FungiBrain), the Agence Nationale de la Recherche (ANR "CellSize"), and the European Research Council (CoG Forcaster No. 647073).

1. S. M. Bowman, S. J. Free, The structure and synthesis of the fungal cell wall. *BioEssays* **28**, 799–808 (2006).
2. D. J. Cosgrove, Growth of the plant cell wall. *Nat. Rev. Mol. Cell Biol.* **6**, 850–861 (2005).
3. T. J. Silhavy, D. Kahne, S. Walker, The bacterial cell envelope. *Cold Spring Harb. Perspect. Biol.* **2**, a000414 (2010).
4. A. Boudaoud, An introduction to the mechanics of morphogenesis for plant biologists. *Trends Plant Sci.* **15**, 353–360 (2010).
5. V. Davi, N. Minc, Mechanics and morphogenesis of fission yeast cells. *Curr. Opin. Microbiol.* **28**, 36–45 (2015).
6. K. C. Huang, R. Mukhopadhyay, B. Wen, Z. Gitai, N. S. Wingreen, Cell shape and cell-wall organization in gram-negative bacteria. *Proc. Natl. Acad. Sci. U.S.A.* **105**, 19282–19287 (2008).
7. N. Minc, A. Boudaoud, F. Chang, Mechanical forces of fission yeast growth. *Curr. Biol.* **19**, 1096–1101 (2009).
8. A. Amir, F. Babaeipour, D. B. McIntosh, D. R. Nelson, S. Jun, Bending forces plastically deform growing bacterial cell walls. *Proc. Natl. Acad. Sci. U.S.A.* **111**, 5778–5783 (2014).
9. E. Rojas, J. A. Theriot, K. C. Huang, Response of Escherichia coli growth rate to osmotic shock. *Proc. Natl. Acad. Sci. U.S.A.* **111**, 7807–7812 (2014).
10. J. F. Abenza *et al.*, Wall mechanics and exocytosis define the shape of growth domains in fission yeast. *Nat. Commun.* **6**, 8400 (2015).
11. E. Atilgan, V. Magidson, A. Khodjakov, F. Chang, Morphogenesis of the fission yeast cell through cell wall expansion. *Curr. Biol.* **25**, 2150–2157 (2015).
12. A. Boudaoud, Growth of walled cells: From shells to vesicles. *Phys. Rev. Lett.* **91**, 018104 (2003).
13. P. Milani, S. A. Braybrook, A. Boudaoud, Shrinking the hammer: Micromechanical approaches to morphogenesis. *J. Exp. Bot.* **64**, 4651–4662 (2013).
14. J. D. Stenson, P. Hartley, C. Wang, C. R. Thomas, Determining the mechanical properties of yeast cell walls. *Biotechnol. Prog.* **27**, 505–512 (2011).
15. D. Bonazzi *et al.*, Symmetry breaking in spore germination relies on an interplay between polar cap stability and spore wall mechanics. *Dev. Cell* **28**, 534–546 (2014).
16. V. Davì *et al.*, Mechanosensation dynamically coordinates polar growth and cell wall assembly to promote cell survival. *Dev. Cell* **45**, 170–182.e7 (2018).
17. E. R. Rojas *et al.*, The outer membrane is an essential load-bearing element in gram-negative bacteria. *Nature* **559**, 617–621 (2018).
18. F. Chang, K. C. Huang, How and why cells grow as rods. *BMC Biol.* **12**, 54 (2014).
19. F. Chang, S. G. Martin, Shaping fission yeast with microtubules. *Cold Spring Harb. Perspect. Biol.* **1**, a001347 (2009).
20. V. Graml *et al.*, A genomic multiprocess survey of machineries that control and link cell shape, microtubule organization, and cell-cycle progression. *Dev. Cell* **31**, 227–239 (2014).
21. J. Hayles *et al.*, A genome-wide resource of cell cycle and cell shape genes of fission yeast. *Open Biol.* **3**, 130053 (2013).
22. A. Haupt, D. Ershov, N. Minc, A positive feedback between growth and polarity provides directional persistency and flexibility to the process of tip growth. *Curr. Biol.* **28**, 3342–3351.e3 (2018).
23. A. Cadou *et al.*, Kin1 is a plasma membrane-associated kinase that regulates the cell surface in fission yeast. *Mol. Microbiol.* **77**, 1186–1202 (2010).
24. T. Andoh, T. Yoko, Y. Matsui, A. Toh, Molecular cloning of the plc1+ gene of Schizosaccharomyces pombe, which encodes a putative phosphoinositide-specific phospholipase C. *Yeast* **11**, 179–185 (1995).
25. A. Sapala *et al.*, Why plants make puzzle cells, and how their shape emerges. *eLife* **7**, e32794 (2018).
26. F. D. Kelly, P. Nurse, De novo growth zone formation from fission yeast spheroplasts. *PLoS One* **6**, e27977 (2011).
27. Y. Zegman, D. Bonazzi, N. Minc, Measurement and manipulation of cell size parameters in fission yeast. *Methods Cell Biol.* **125**, 423–436 (2015).
28. D. Bonazzi *et al.*, Actin-based transport adapts polarity domain size to local cellular curvature. *Curr. Biol.* **25**, 2677–2683 (2015).
29. D. Kierzkowski *et al.*, Elastic domains regulate growth and organogenesis in the plant shoot apical meristem. *Science* **335**, 1096–1099 (2012).
30. Y. Nakayama, K. Yoshimura, H. Iida, Organellar mechanosensitive channels in fission yeast regulate the hypo-osmotic shock response. *Nat. Commun.* **3**, 1020 (2012).
31. P. Pérez, J. Cansado, Cell integrity signaling and response to stress in fission yeast. *Curr. Protein Pept. Sci.* **11**, 680–692 (2010).
32. L. Mukaremera *et al.*, Titan cell production in *Cryptococcus neoformans* reshapes the cell wall and capsule composition during infection. *Cell Surf.* **1**, 15–24 (2018).
33. L. S. Ryder, N. J. Talbot, Regulation of appressorium development in pathogenic fungi. *Curr. Opin. Plant Biol.* **26**, 8–13 (2015).
34. Y. Deng, M. Sun, J. W. Shaevitz, Direct measurement of cell wall stress stiffening and turgor pressure in live bacterial cells. *Phys. Rev. Lett.* **107**, 158101 (2011).
35. O. Campàs, L. Mahadevan, Shape and dynamics of tip-growing cells. *Curr. Biol.* **19**, 2102–2107 (2009).
36. T. Drake, D. Vavylonis, Model of fission yeast cell shape driven by membrane-bound growth factors and the cytoskeleton. *PLoS Comput. Biol.* **9**, e1003287 (2013).